Electronic Supplementary Material (ESI) for Green Chemistry.

SUPPLEMENTARY INFORMATION

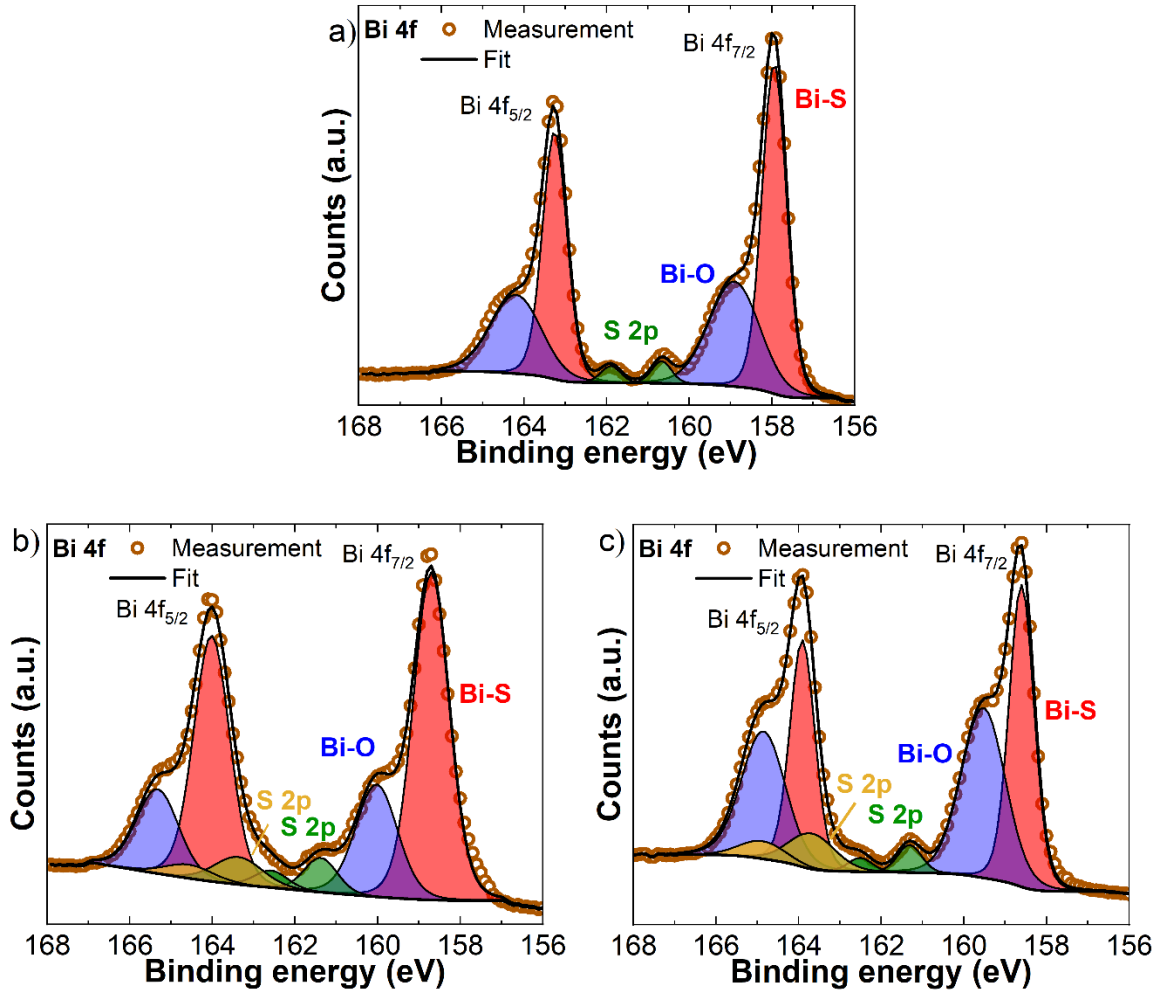

Figure S1 High resolution, Bi 4f core spectrum of a) pristine Bi_2S_3 nanocrystals, b) HC-MPA/5BS, and c) HC-MPA/10BS.

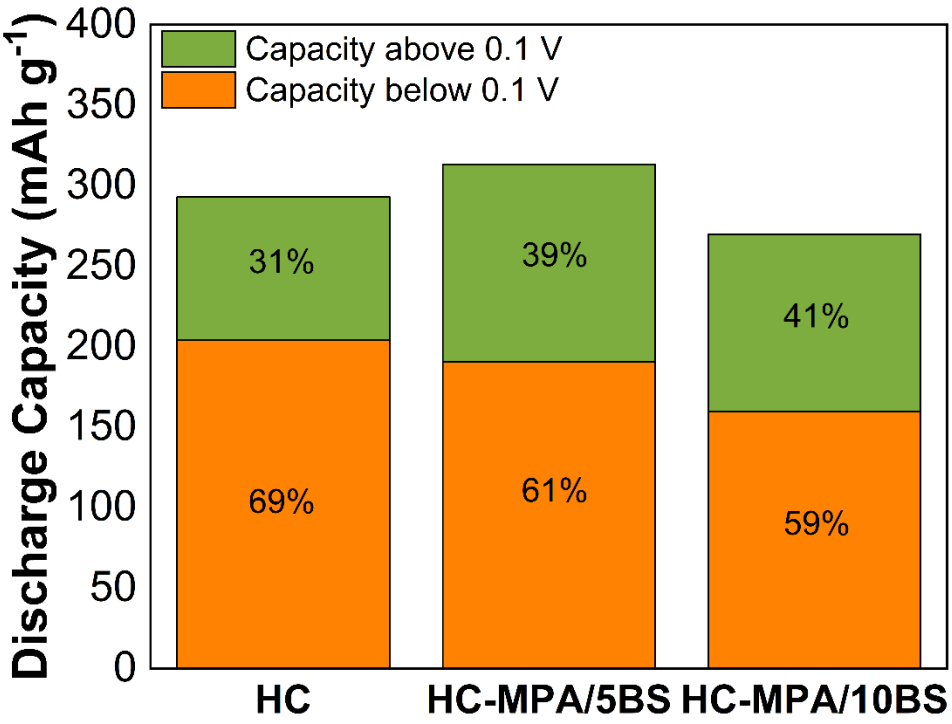

Figure S2 Capacity contributions for the fifth cycles of HC, HC-MPA/5BS, and HC-MPA/10BS.

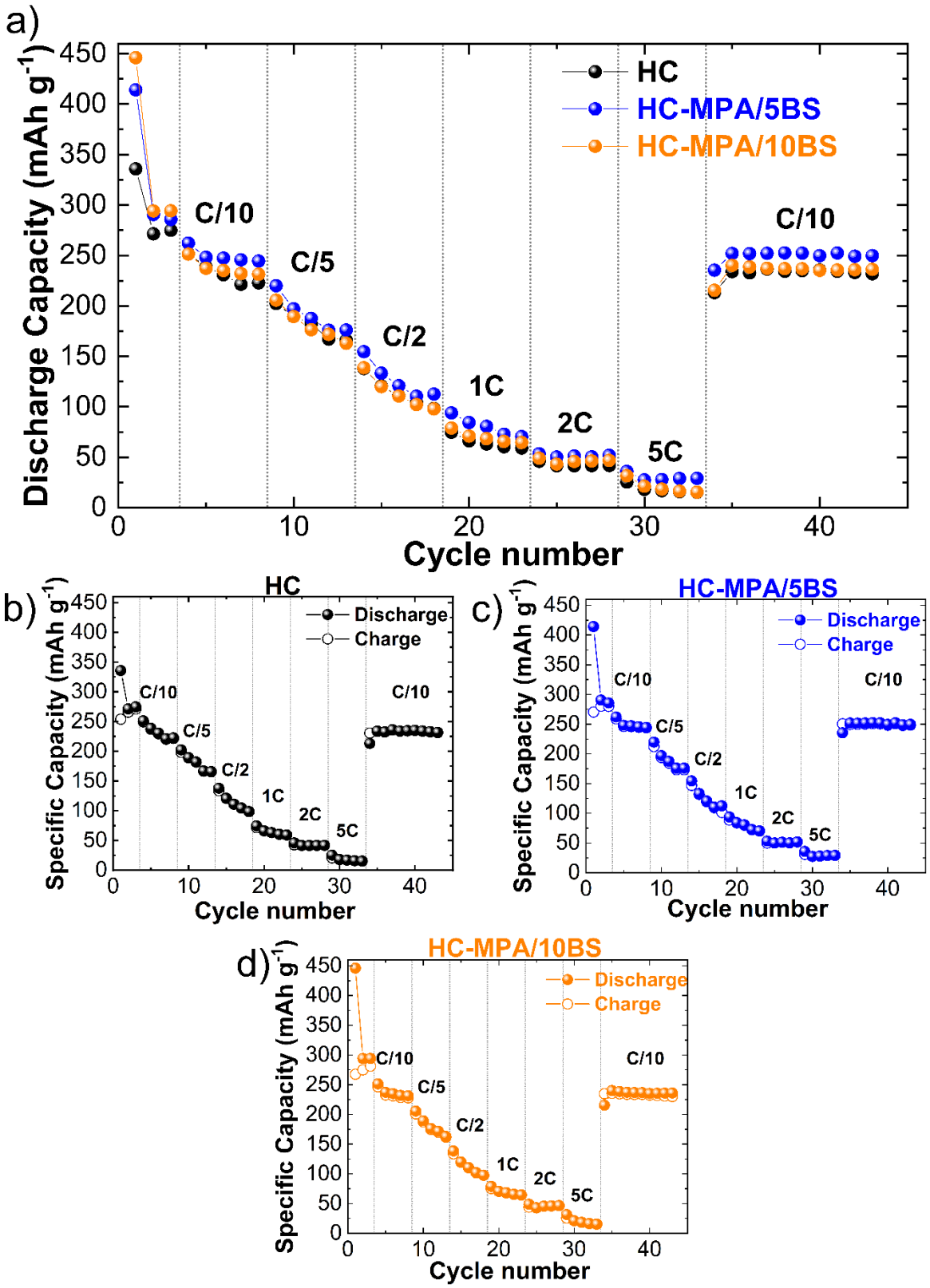

Figure S3 a) Discharge capacities of rate performance of HC, HC-MPA/5BS, and HC-MPA/10BS. Specific capacities of b) HC, c) HC-MPA/5BS, and d) HC-MPA/10BS.

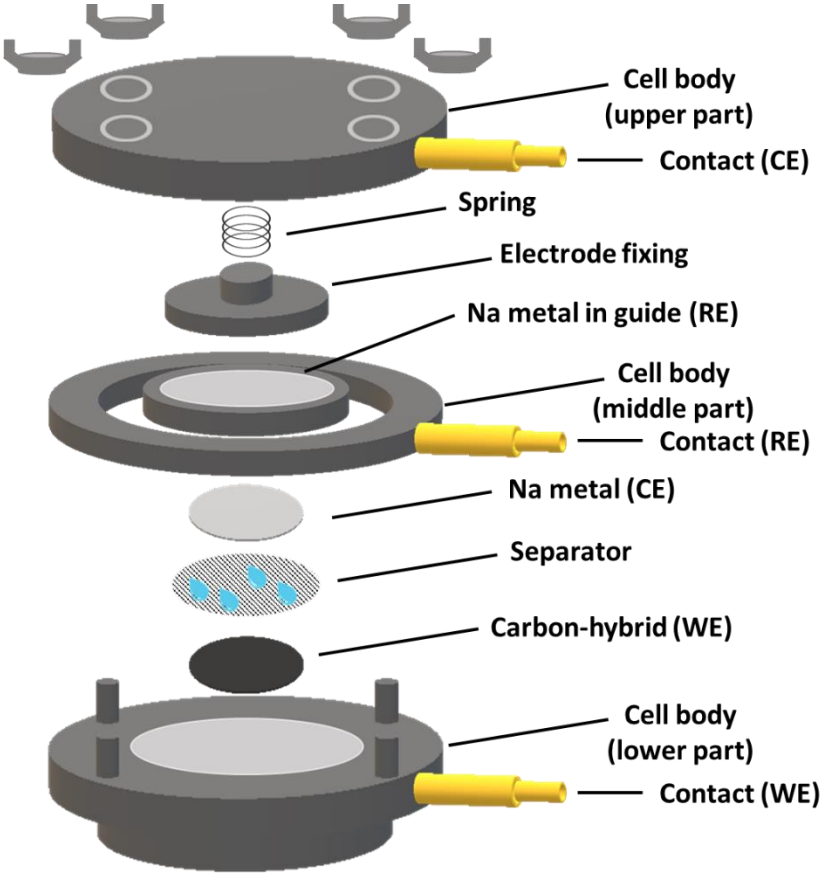

Figure S4 Three-electrode cell setup.

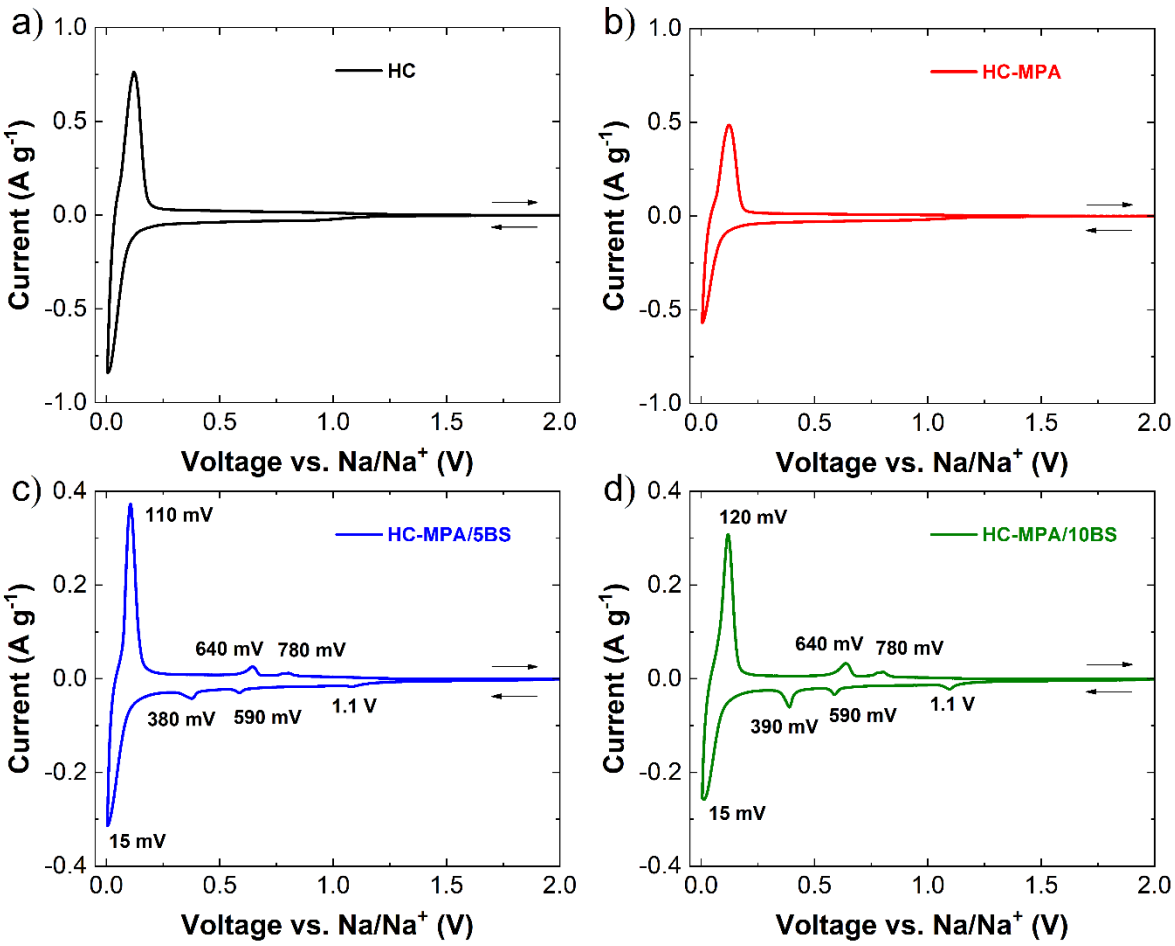

Figure S5 Cyclic voltammograms of a) HC, b) HC-MPA, c) HC-MPA/5BS, and d) HC-MPA/10BS. Measurements were performed in a three-electrode cell with sodium metal as the reference electrode at the sweep rate of 0.1 mV s^{-1}.

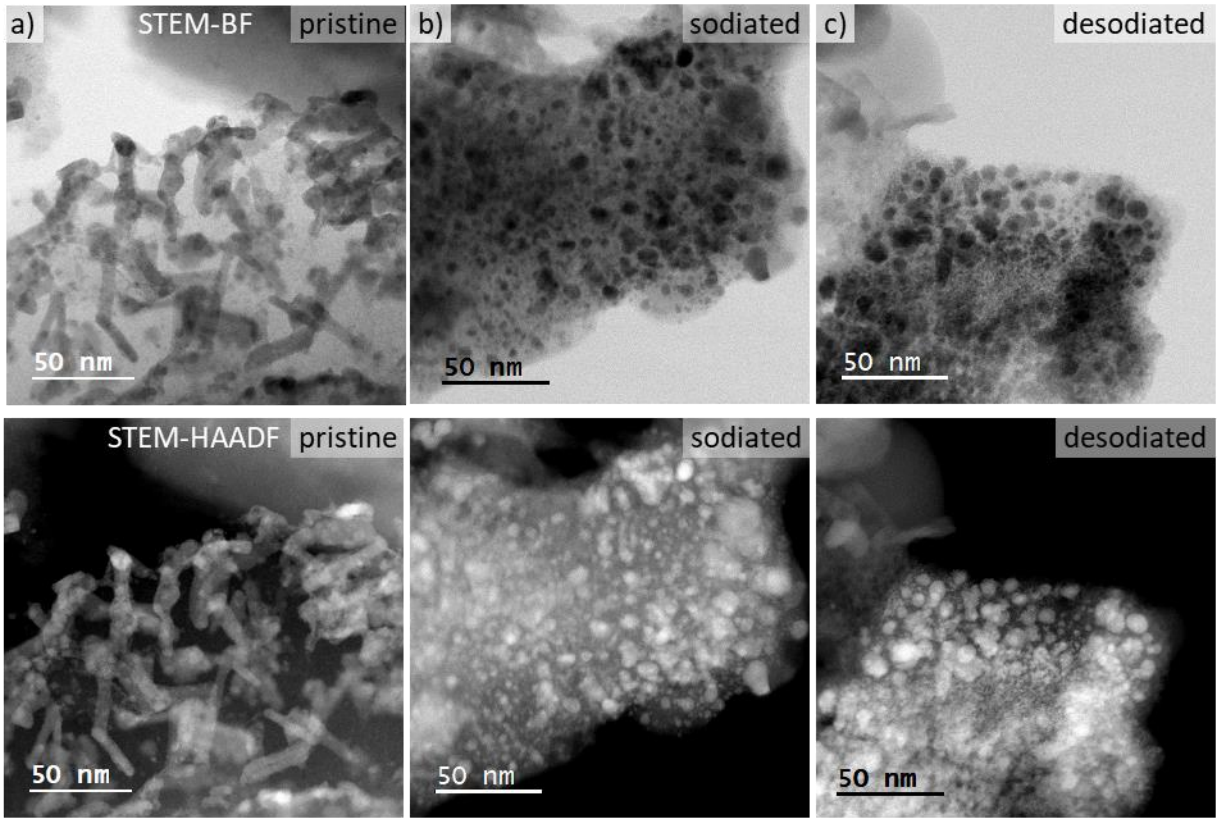

Figure S6 STEM images of HC-MPA/10BS at lower magnifications, in a) pristine, b) sodiated, and c) desodiated state.

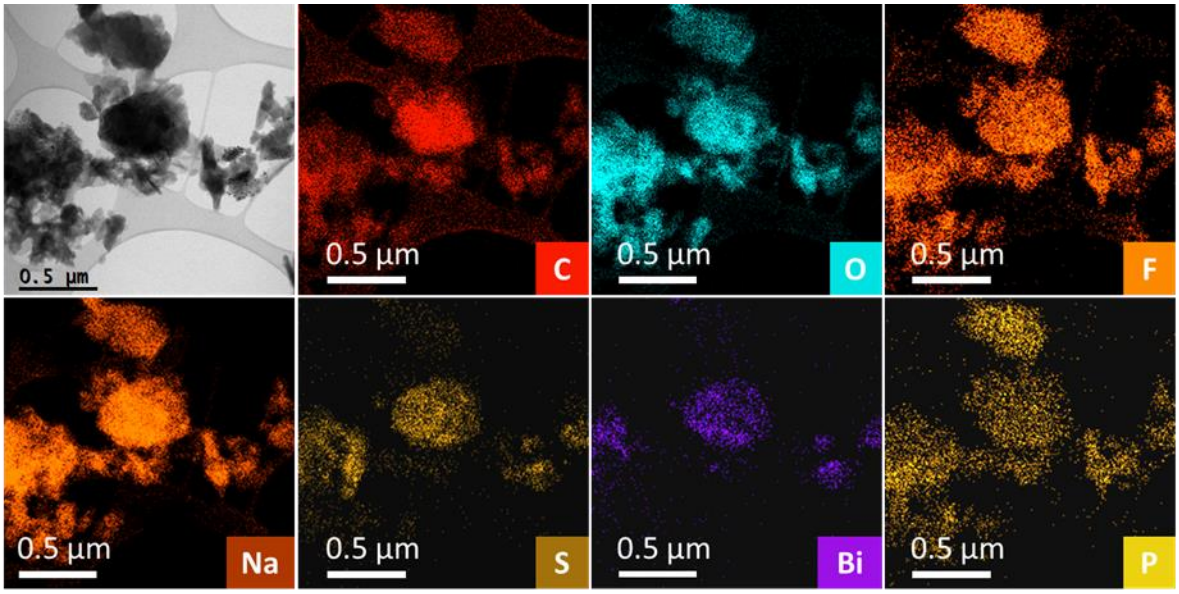

Element	Atom %	σ
C	57.1	0.2
O	17.6	0.2
F	6.1	0.1
Na	18.1	0.2
P	0.5	0.1
S	0.4	0.1
Bi	0.2	0.1
Total	100	/

Figure S7 EDX imaging and quantification of HC-MPA/10BS in the sodiated state.

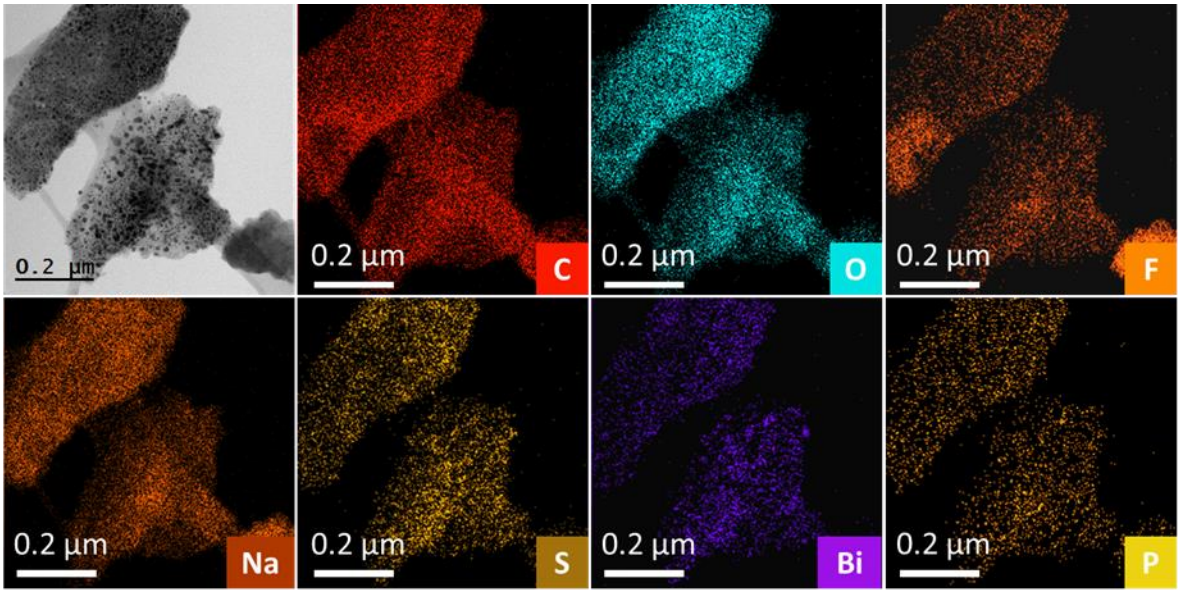

Element	Atom %	σ
C	69.3	0.2
O	10.1	0.2
F	5.3	0.1
Na	14.0	0.2
P	0.2	0.1
S	0.3	0.1
Bi	0.8	0.1
Total	100	/

Figure S8 EDX imaging and quantification of HC-MPA/10BS in the desodiated state.

Table S1 Example of d spacing differences for structures present upon sodiation and desodiation. Values are given in Angstroms.

Bi_2S_3 - ICDD: 00-043-1471				**Bi** - ICDD: 00-001-0688				**NaBi** - ICDD: 03-065-2805				**Na_3Bi**- ICDD: 04-003-7088				**Na_2S** - ICDD: 01-070-7161			
h	k	l	d	h	k	l	d	h	k	l	d	h	k	l	d	h	k	l	d
2	0	0	5.379	0	0	3	3.954	0	0	1	4.000	0	0	1	9.000	1	0	0	6.000
0	0	2	5.325	1	0	1	3.745	1	0	0	3.000	0	0	2	4.500	1	1	0	4.243
2	0	1	4.801	1	0	4	2.731	1	0	1	2.400	1	0	0	4.330	1	1	1	3.464
1	0	2	4.772	1	1	0	2.279	1	1	0	2.121	1	0	1	3.902	2	0	0	3.000
0	1	0	3.883	0	0	6	1.977	0	0	2	1.664	1	0	2	3.120	2	1	0	2.683
2	0	2	3.784	1	1	3	1.974	1	1	1	1.874	0	0	3	3.000	2	1	1	2.449
1	1	0	3.653	2	0	2	1.872	1	0	2	1.664	1	1	0	2.500	2	2	0	2.121
0	1	1	3.648	1	0	7	1.557	2	0	0	1.500	1	0	3	2.466	2	2	1	2.000
3	0	0	3.586	2	0	5	1.517	1	1	2	1.455	1	1	1	2.409	3	0	0	2.000
0	0	3	3.550	1	1	6	1.493	2	0	1	1.404	0	0	4	2.250	3	1	0	1.897
1	1	1	3.455	2	1	1	1.480	2	1	0	1.342	1	1	2	2.185	3	1	1	1.809
3	0	1	3.399	2	1	4	1.333	0	0	3	1.333	2	0	0	2.165	2	2	2	1.732
1	0	3	3.371	0	0	9	1.318	2	1	1	1.272	2	0	1	2.105	3	2	0	1.664
2	1	0	3.149	3	0	0	1.315	1	0	3	1.218	1	0	4	1.997	3	2	1	1.604
0	1	2	3.138	3	0	3	1.248	2	0	2	1.200	2	0	2	1.951	4	0	0	1.500
2	1	1	3.019	2	0	8	1.185	1	1	3	1.129	1	1	3	1.921	3	2	2	1.455
1	1	2	3.012	1	1	9	1.141	2	1	2	1.114	0	0	5	1.800	4	1	0	1.455
3	0	2	2.974	2	2	0	1.139	2	2	0	1.061	2	0	3	1.756	3	3	0	1.414
2	0	3	2.974	1	0	10	1.136	2	2	1	1.025	1	1	4	1.672	4	1	1	1.414
2	1	2	2.710	2	1	7	1.120	0	0	4	1.000	1	0	5	1.662	3	3	1	1.376
4	0	0	2.690	3	0	6	1.095	3	0	0	1.000	2	1	0	1.637	4	2	0	1.342

Note 1 – Hybrid HC/BS materials without MPA bonding-enhancing agent

Concerning the hybrid HC/BS materials, the X-ray diffraction (XRD) patterns closely resemble those of HC-MPA/BS, as depicted in Figure S9a. Peaks corresponding to the Bi_2S_3 nanocrystals align well with the reference pattern, validating their presence. Notably, in the case of HC/10BS, the Bi_2S_3 peaks are more prominent, attributed to the higher loading of Bi_2S_3 nanocrystals.

TG analysis was carried out following the same method and calculations outlined in the main article (Figure S9b). When subjected to air atmosphere, the calcination of HC takes place within the 400-600°C range, resulting in an inorganic residual mass primarily composed of potassium and silicon.[1] Similar observations are noted for HC/5BS, with additional residual mass due to Bi_2O_3 formation. In contrast, HC/10BS displays a split in the TG curve between 400°C and 600°C, indicative of the oxidation process of sulfide species, similar to HC-MPA/10BS.[2] Additionally, HC/BS materials showcase lower degradation temperatures compared to their MPA-treated counterparts due to the absence of organic molecules on the carbon surface.[3,4] As a result, the final weight fractions for HC/5BS and HC/10BS amount to 4.4 wt.% and 7.7 wt.%, respectively, lower than those observed for HC-MPA/BS materials.

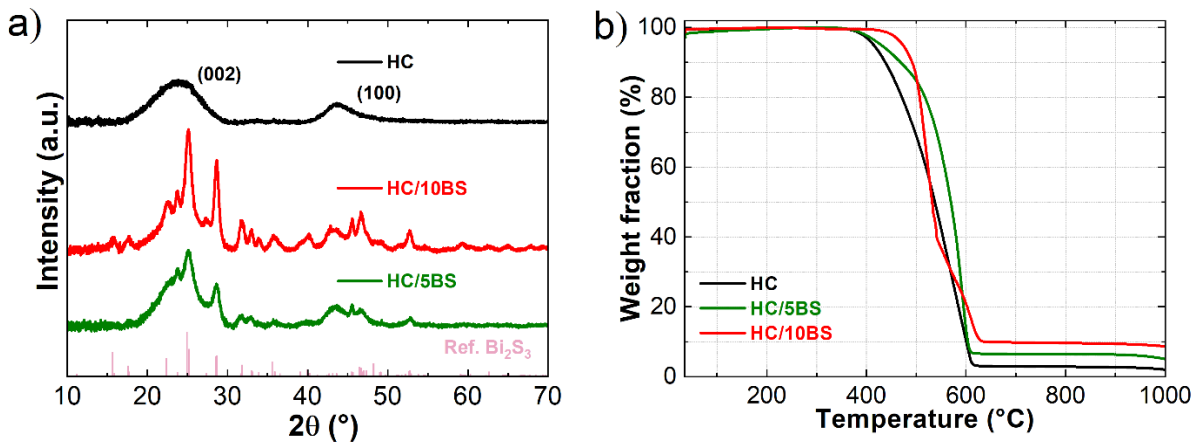

Figure S9 a) XRD patterns HC/BS (Bi_2S_3 reference is added for comparison - ICDD: 00-043-1471), and b) TG analysis of HC/BS.

The interaction between Bi_2S_3 nanocrystals and the carbon surface was investigated using high-resolution Bi 4*f* XPS. Analogous to HC-MPA/BS, the Bi 4*f* components demonstrate doublets Bi $4f_{5/2}$ and Bi $4f_{7/2}$ due to spin-orbit coupling. Analysis of the HC/5BS Bi $4f_{7/2}$ spectrum reveals the Bi–S bond at 157.9 eV and the Bi–O bond at 158.9 eV (Figure S10a). Notably, a more pronounced Bi-O curve is evident compared to HC-MPA/BS materials, resulting in an increased Bi–O/Bi–S ratio of 2.2. This underscores bismuth's affinity for bonding with oxygen groups on the carbon surface.[5,6] Furthermore, the S 2*p* region displays two peaks at 161.9 eV and 160.7 eV, corresponding to doublets $2p_{1/2}$ and $2p_{3/2}$, respectively. A similar trend is observed in the HC/10BS spectrum (Figure S10b).

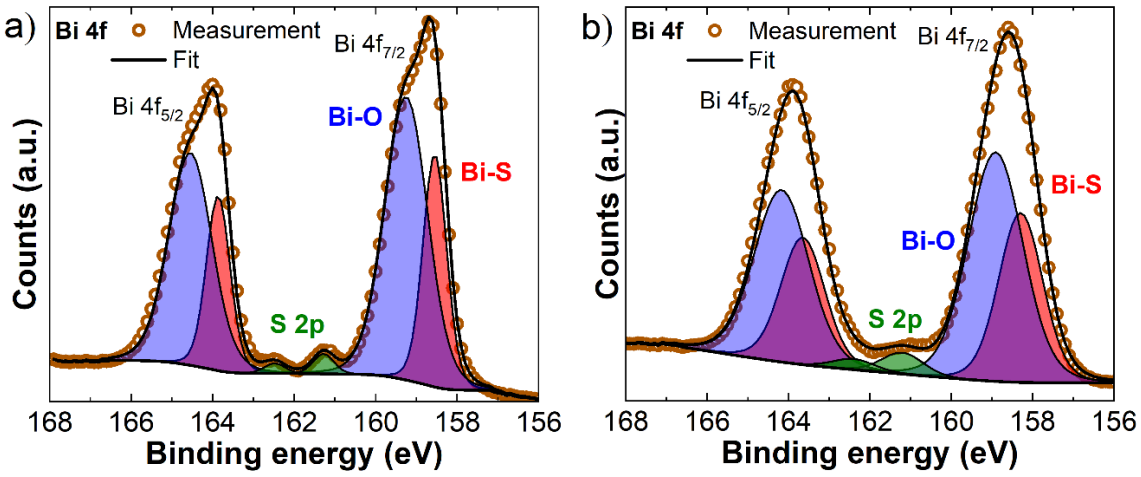

Figure S10 High resolution, Bi 4f core spectrum of a) HC/5BS and b) HC/10BS.

The half-cell electrochemical performance of HC/BS is depicted in Figure S11a. Much like HC-MPA/BS, two distinct plateaus are evident in the high voltage region, reflecting the phase reaction of sodium with Bi_2S_3 nanocrystals, while a plateau associated with hard carbon's charge storage processes is evident in the low voltage region. In both instances, the capacity contribution from the high voltage region demonstrates a notable increase compared to HC. This trend is more clearly visualized in Figure S12, where the capacity contribution from the sloping region elevates from 31% to 35% and eventually to 40% for HC, HC/5BS, and HC/10BS, respectively.

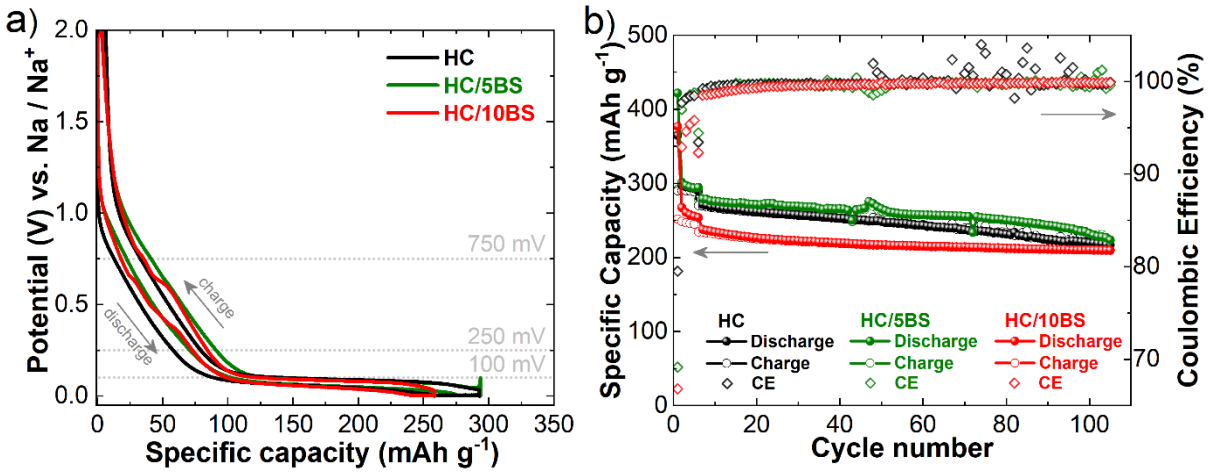

Figure S 11 a) Electrochemical curves of the fifth formation cycle, and b) prolonged cycling of HC/BS. Charge/discharge capacities are presented on the left Y-axis and Coulombic efficiency is presented on the right Y-axis. Five formation cycles were performed with the current rate of C/10 followed by 100 cycles at 1C. A constant voltage step was applied at the lower cut-off of 5 mV.

Figure S11b portrays the extended cycling outcomes of HC, HC/5BS, and HC/10BS. Noteworthy is the high initial discharge capacity of 422 mAh g^{-1} observed for HC/5BS, while HC/10BS displays a slightly lower capacity of 377 mAh g^{-1}. Similar to HC-MPA/BS, both HC/5BS and HC/10BS demonstrate low initial Coulombic efficiencies (ICEs) of 69% and 67%, respectively. Under a higher current density of 1C, the Bi_2S_3 nanocrystal-modified carbons demonstrate relatively minor capacity degradation. After 100 cycles, final capacities of 217 mAh g^{-1}, 224 mAh g^{-1}, and 210 mAh g^{-1} are

observed for HC, HC/5BS, and HC/10BS, respectively. Interestingly, the capacity improvement with a 5% addition of Bi_2S_3 is marginal, whereas the addition of 10% Bi_2S_3 demonstrates detrimental behavior once more.

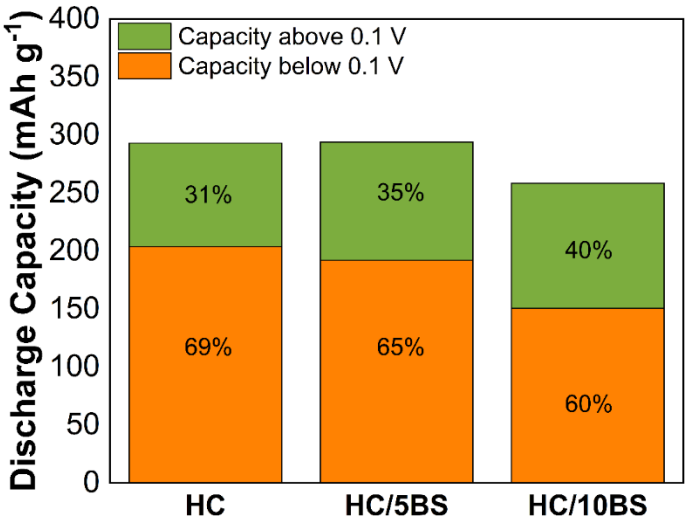

Figure S12 Capacity contributions for the fifth cycles of HC, HC/5BS, and HC/10BS.

Using three-electrode CV measurements, the kinetic constraints of the unmodified HC were assessed. HC demonstrates a single peak during both reduction and oxidation (Figure S13). The reduction shows a b value of 0.422, while during oxidation, it decreases to 0.361. This mirrors the findings observed in HC-MPA/BS, where transport limitations induce a voltage shift to higher levels, concurrently reducing the b value during oxidation. These shared characteristics across both scenarios strongly indicate diffusion as the constraining process.

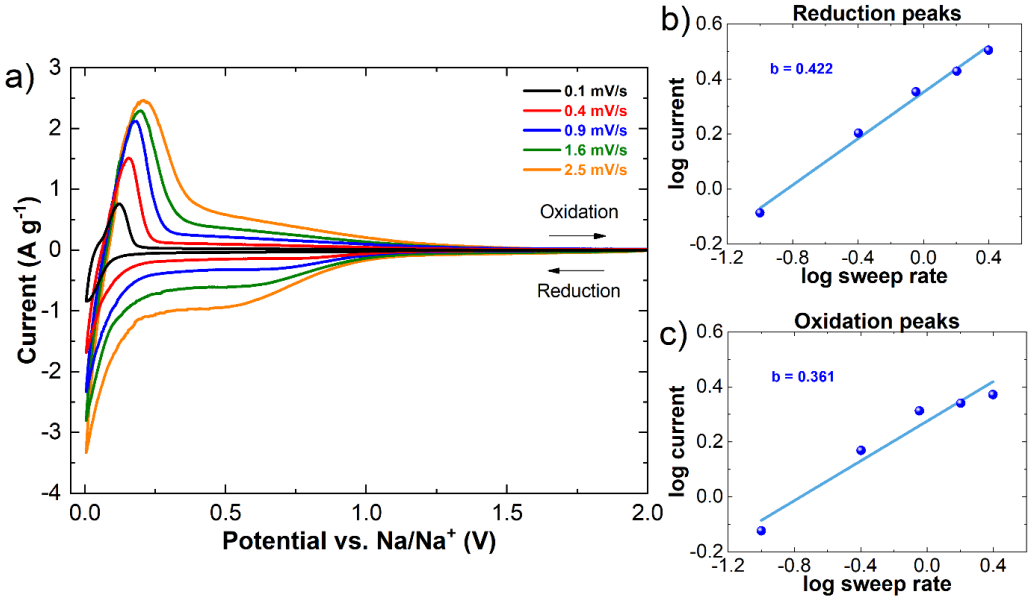

Figure S13 Three-electrode cyclic voltammetry measurements of HC: a) current responses at different scan rates, b) determination of the parameter b for the reduction peak, and c) determination of the parameter b for the oxidation peak.

Note 2 – Three-electrode cyclic voltammetry measurements

The total capacity obtained from a specific material can be divided into different contributions, more specifically the contributions from surface-driven processes such as adsorption and pseudocapacitance and contributions from diffusion-limited processes such as intercalation or pore filling. According to Lindstrom[7] the nature of the individual process can be determined through the current response at different sweep rates, following the power-law relationship (Eq S1):

$$i = a * v^b \quad \text{(Eq. S1)}$$

Parameter *a* is a constant while *b* is a power-law exponent. By experimentally determining parameter *b*, charge storage behavior can be established. For *b*=1, the prevailing processes are surface driven. Meanwhile, diffusion-limited processes exhibit *b* value of 0.5. The value of *b* between 0.5 and 1 indicates the combination of both processes.[8]

Parameter *b* can be determined by the logarithmization of Eq. S2:

$$\log(i) = \log(a) + b * \log(v) \quad \text{(Eq. S2)}$$

Finally, *b* is obtained as the slope of the linearized plot of Eq.S2.

Three-electrode cyclic voltammetry measurements were performed at 5 different sweep rates, namely 0.1, 0.4, 0.9, 1.6, and 2.5 mV $s^{-1,}$ and the current response was measured.

Note 3 – *Ex-situ* TEM measurements

Ex-situ TEM analysis was conducted to observe alterations in Bi_2S_3 nanocrystals throughout multiple sodiation and desodiation stages. Two Swagelok-type cells were assembled in an argon-filled glovebox with water and oxygen contents below 0.5 ppm. HC-MPA/10BS powder was used as the working electrode and sodium metal was used as the counter electrode. The powder and sodium metal were separated by two glass fiber separators (GF-A), wetted by 150 µl of 1M $NaPF_6$ in EC: DMC (1:1 vol.%) + 2 wt.% FEC. The cells were cycled in a voltage range between 2 V and 0.005 V vs Na/Na^+ with the current of 30 mA g^{-1} (C/10) in the discharge (sodiation) and the current of 10 mA g^{-1} (C/30) in the charge (desodiation) step as presented in Figure S13. A slower rate was used during charging to suppress the formation of dendrites on the sodium metal electrode. The first cell was stopped after the 5th discharge while the second cell was stopped after the 5th charge step. The cells were then transferred to a glovebox and disassembled. The HC-MPA/10BS powder was recovered from both cells and washed with DMC.

TEM samples were prepared by mixing approximately 800 µg of the powder in 5 mL of toluene in a vial. The vials were then sealed with parafilm and taken outside of the glovebox to disperse the powder in an ultrasonic bath for 15 min. The vials were returned to the glovebox where 20 µL of the suspension was placed on the copper TEM grid. Copper grids were transferred to the TEM microscope with a vacuum transfer grid.

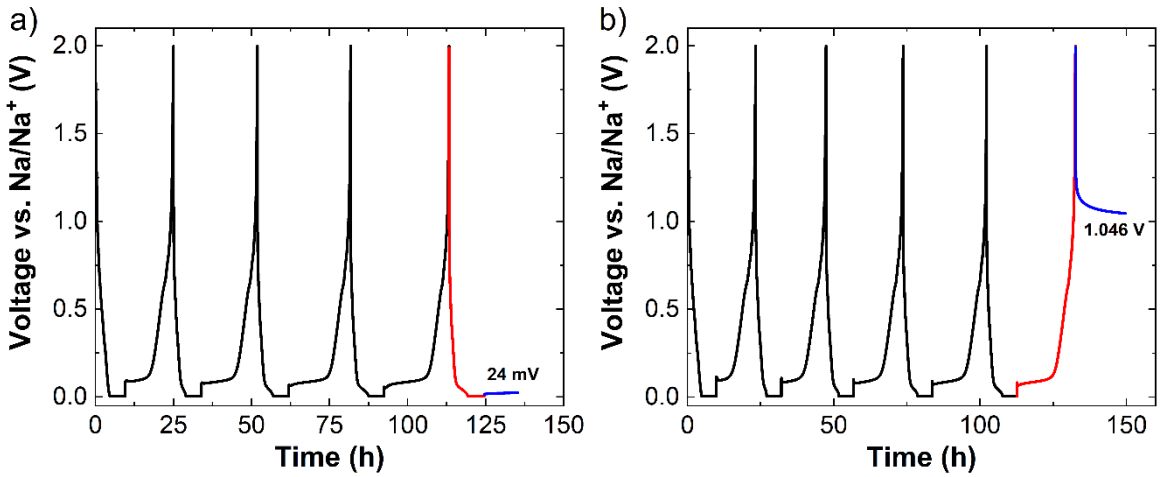

Figure S14 Voltage profile of HC-MPA/10BS powder stopped after a) 5th discharge and b) 5th charge.

Note 4 – *Operando* X-ray diffraction measurements

Operando X-ray diffraction measurements were performed in the range of 2θ from 16° to 50° with a step of 0.038° and a measurement time of 1.9s per step. The total time per scan amounted to 31.5 minutes. Electrodes with a composition of 85 wt.% HC-MPA/10BS, 5 wt.% SuperC65 (Timcal) and 10 wt.% polytetrafluoroethylene (PTFE, Aldrich) were fabricated. Carbon composite electrodes were used as the working electrode whereas sodium metal (Aldrich) was used as the counter electrode. The electrodes were separated by two glass fiber separators (Whatman GF-A). The electrolyte used was 1M $NaPF_6$ in EC: DMC (1:1 vol.%) + 2 wt.% FEC. A total of 300 µl of the electrolyte was distributed between the electrodes and both separators. Electrochemical measurements were carried out within a potential window between 2 V and 0.005 V vs Na/Na^+ with a current of 10 mA g^{-1} (C/30). At the end of sodiation a constant voltage step was applied at the lower cut-off, limited to 5 h or until the current rate was lower than C/100. Electrochemical measurements were performed in an electrochemical cell described in detail by Leriche et al.[9]

Figure S15 presents a contour plot illustrating *operando* XRD measurements, comparing the behavior of HC with HC-MPA/10BS. In HC, a distinct broad peak around 23° is detected, representing the (002) planes of stacked graphene sheets before sodiation begins. Notably, a decrease in peak intensity is observed as sodiation progresses, particularly pronounced in the low voltage plateau region. This decline in intensity, as suggested by Beda et al.[10], indicates a transition to a more disordered state within the hard carbon structure due to Na^+ ion intercalation. Conversely, in HC-MPA/10BS, the broad carbon peak is not discernible in the contour plot due to its overlap with Bi_2S_3-related peaks. Throughout sodiation, the Bi_2S_3 phase gradually transforms into the Na_3Bi alloy, with the most pronounced Na_3Bi peaks at 20° and 23° observed during the second high voltage plateau. The intensity of these peaks decreases as Na^+ ions intercalate into the hard carbon structure, but regains intensity during deintercalation. Notably, at the end of sodiation, the original Bi_2S_3 phase is not recovered. Thus, while conventional XRD methods cannot determine other Na^+ ion interactions with hard carbon active sites, the observed changes in peak intensity provide valuable insights into the structural transitions occurring during the electrochemical processes.

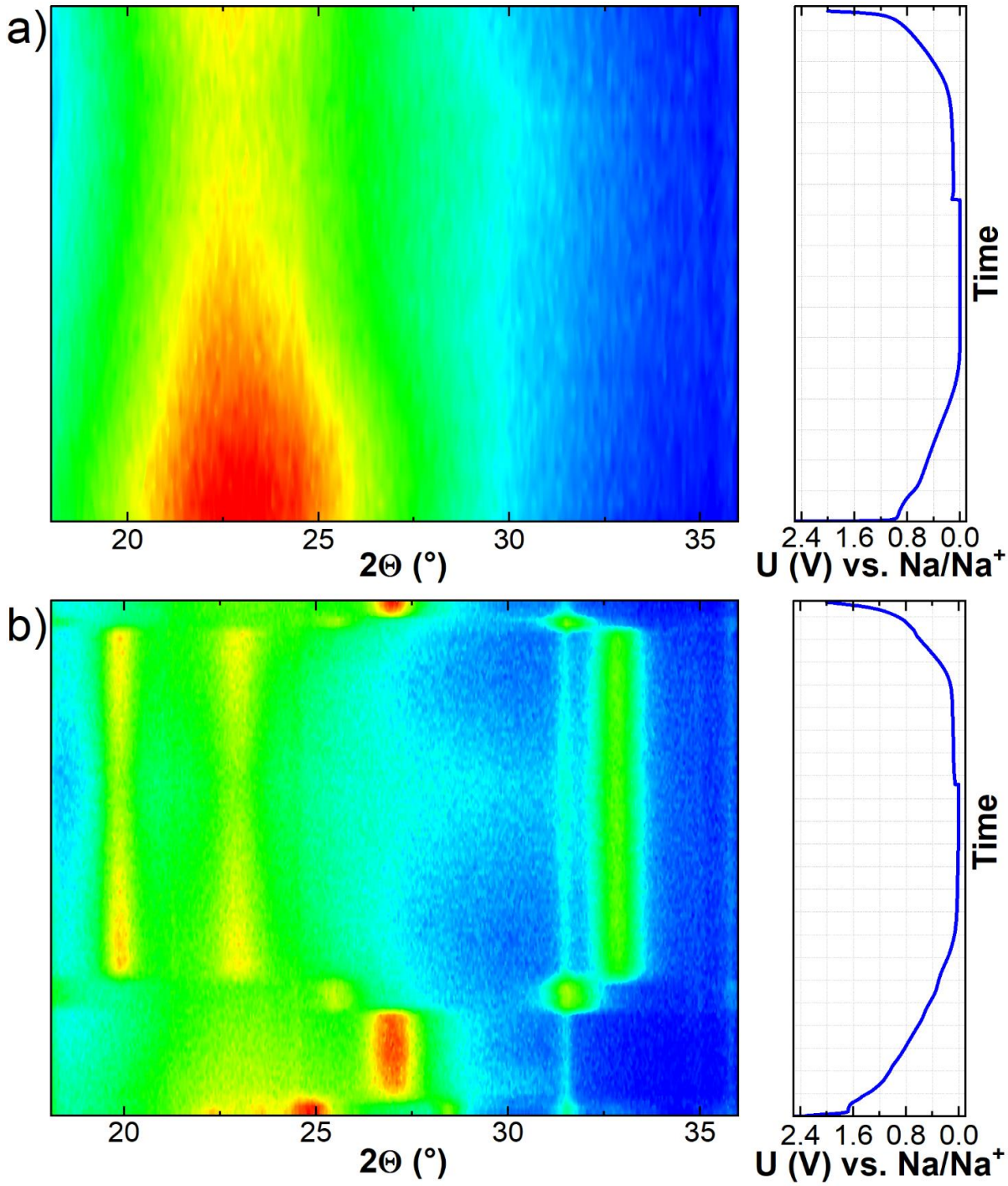

Figure S15 Contour plot of operando XRD during sodiation/desodiation of a) HC and b) HC-MPA/10BS. The dark blue color corresponds to the lowest intensity, while the red color corresponds to the highest intensity.

References

1 B. Tratnik, N. Van de Velde, I. Jerman, G. Kapun, E. Tchernychova, M. Tomšič, A. Jamnik, B. Genorio, A. Vizintin and R. Dominko, *ACS Appl Energy Mater*, 2022, **5**, 10667–10679.

2 T. K. Patil, *Pelagia Research Library Advances in Applied Science Research*, 2013, 4, 115–122.

3 S. Bahçeci Sertkol, B. Esat, A. A. Momchilov, M. Burak Yılmaz and M. Sertkol, *Carbon*, 2017, **116**, 154–166.

4 Z. Du, W. Ai, L. Xie and W. Huang, *J Mater Chem A Mater*, 2014, **2**, 9164.

5 N. G. García-Peña, D. Díaz, G. Rodríguez-Gattorno, I. Betancourt and I. Zumeta-Dubé, *Mater Chem Phys*, 2018, **219**, 376–389.

6 C. Qu, H. Li, S. Zhou, G. Li, C. Wang, R. Snyders, C. Bittencourt and W. Li, *Chemosensors*, 2021, **9**, 190.

7 H. Lindström, S. Södergren, A. Solbrand, H. Rensmo, J. Hjelm, A. Hagfeldt and S.-E. Lindquist, *J Phys Chem B*, 1997, **101**, 7717–7722.

8 C. Choi, D. S. Ashby, D. M. Butts, R. H. DeBlock, Q. Wei, J. Lau and B. Dunn, *Nat Rev Mater*, 2020, 5, 5–19.

9 J. B. Leriche, S. Hamelet, J. Shu, M. Morcrette, C. Masquelier, G. Ouvrard, M. Zerrouki, P. Soudan, S. Belin, E. Elkaïm and F. Baudelet, *J Electrochem Soc*, 2010, **157**, A606.

10 A. Beda, C. Villevieille, P.-L. Taberna, P. Simon and C. Matei Ghimbeu, *J Mater Chem A Mater*, 2020, **8**, 5558–5571.